SCIENCE CHINA
Chemistry

•ARTICLES•

https://doi.org/10.1007/s11426-019-9620-1

Integrating photocatalytic reduction of CO_2 with selective oxidation of tetrahydroisoquinoline over InP–In_2O_3 Z-scheme p-n junction

Bohang Zhao[1], Yi Huang[1], Dali Liu[1], Yifu Yu[1,2] & Bin Zhang[1,3*]

[1]*Department of Chemistry, Tianjin Key Laboratory of Molecular Optoelectronic Sciences, School of Science, Tianjin University, Tianjin 300072, China;*
[2]*Institute of Molecular Plus, Tianjin University, Tianjin 300072, China;*
[3]*Collaborative Innovation Center of Chemical Science and Engineering, Tianjin 300072, China*

Received July 15, 2019; accepted September 20, 2019; published online November 18, 2019

The development of a facile strategy to construct stable hierarchal porous heterogeneous photocatalysts remains a great challenge for efficient CO_2 reduction. Additionally, hole-trapping sacrificial agents (e.g., triethanolamine, triethylamine, and methanol) are mostly necessary, which produce useless chemicals, and thus cause costs/environmental concerns. Therefore, utilizing oxidation ability of holes to develop an alternative photooxidation reaction to produce value-added chemicals, especially coupled with CO_2 photoreduction, is highly desirable. Here, an *in situ* partial phosphating method of In_2O_3 is reported for synthesizing InP–In_2O_3 p-n junction. A highly selective photooxidation of tetrahydroisoquinoline (THIQ) into value-added dihydroisoquinoline (DHIQ) is to replace the hole driven oxidation of typical sacrificial agents. Meanwhile, the photoelectrons of InP–In_2O_3 p-n junction can induce the efficient photoreduction of CO_2 to CO with high selectivity and stability. The evolution rates of DHIQ and CO are 2 and 3.8 times higher than those of the corresponding In_2O_3 n-type precursor, respectively. *In situ* irradiated X-ray photoelectron spectroscopy and electron spin resonance are utilized to confirm that the direct Z-scheme mechanism of InP–In_2O_3 p-n junction accelerate the efficient separation of photocarriers.

CO_2 reduction, dehydrogenation, photocatalysis, Z-scheme, tetrahydroisoquinoline

Citation: Zhao B, Huang Y, Liu D, Yu Y, Zhang B. Integrating photocatalytic reduction of CO_2 with selective oxidation of tetrahydroisoquinoline over InP–In_2O_3 Z-scheme p-n junction. *Sci China Chem*, 2019, 62, https://doi.org/10.1007/s11426-019-9620-1

1 Introduction

Photocatalytic reduction of CO_2 (PRC) is a promising way to convert greenhouse gas into fuels and useful chemical materials [1–7], and thus provides a possible way to solve the global energy crisis and environmental problems [8–12]. Currently, increasing efforts have been devoted to the exploration of suitable semiconductors (e.g., metal oxides [13–16], oxynitrides [17], phosphides [4,18], sulphides [19] and metal complexes [20–22]) as photocatalysts for PRC. For instance, porous and hierarchal features are engineered into photocatalytic nanomaterials for enhancing photoadsorption and accelerating photocarrier separation [23–26]. Growing another appropriate material on pure semiconductors to produce Type I, Type II and Z-scheme hybrid photocatalysts is effective for promoting the charge separation efficiency [27–30]. However, the rational design of heterostructured photocatalysts endowing porous and hierarchal characteristics is still challenging [31]. In addition, for most typical methods, the lattice mismatches between heterostructures often lead to weak interface stability and interfacial inactivation [32]. Thus, it is highly desirable to develop a facile

*Corresponding author (email: bzhang@tju.edu.cn)

strategy to synthesize heterogeneous materials with porous and hierarchical architectures for PRC.

Sacrificial agents are often adopted to trap photogenerated holes during PRC measurements because of the high oxidation potential of water [33,34]. Although the addition of sacrificial agents (e.g., triethanolamine, triethylamine, and methanol) can boost the performance of PRC, this process inevitably increase costs and cause environmental concerns. Thus, effective utilization of photoinduced holes for catalytic oxidation synthesis of value-added chemicals to replace useless sacrificial agents is of vital importance [35–38].

Dihydroisoquinoline (DHIQ) and its derivatives, ones of important intermediates in pharmaceuticals and fine chemicals [39,40], are typically synthesized by the well-designed multi-component multistep process [41] or noble metal catalyzed dehydrogenation of corresponding tetrahydroisoquinoline (THIQ) precursors [42,43]. However, the complex process or the use of noble metal restricts their practical applications. Impressively, THIQ owns a lower oxidation potential than water, providing rich possibility for using THIQ to replace conventional sacrificial agents during PRC. Therefore, a selective photooxidation of cheap THIQ to value-added DHIQ, especially integrated with efficient PRC, is economically desirable.

Here, by using n-type In_2O_3 nanosheet-based porous hierarchical spheres as the starting materials, we report an *in situ* partial phosphating method to synthesize InP–In_2O_3 p-n junction (Figure 1). By coupling PRC with the dehydrogenation of THIQ, the conversion efficiency of PRC into CO can be boosted, meanwhile, the DHIQ with an outstanding selectivity can be obtained. Moreover, DHIQ derivatives can be accessible by integrating with PRC. Furthermore, the Z-scheme mechanism of InP–In_2O_3 p-n junction is found to be important for accelerating the separation of electrons and holes, making their performance much higher than those of starting In_2O_3.

2 Experimental

2.1 Chemicals

Indium chloride ($InCl_3$), L-cysteine, triethylenetetramine (TETA) were purchased from Aladdin Ltd. (China). Sodium hypophosphite, anhydrous magnesium sulfate and triethanolamine (TEOA) were purchased from JK Chemical Ltd. (China). Tetrahydroisoquinoline derivatives was purchased from Bide Pharmatech Ltd. (China). The carbon dioxide (CO_2) gas was bought from Air Liquide (Tianjin) Co., Ltd. (China). Deionized water (DIW) was used in all the experimental processes. All chemicals were of analytical grade and used without further purification.

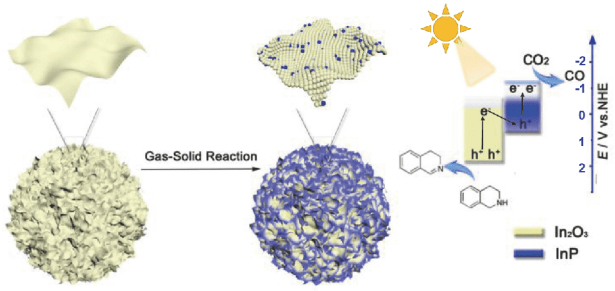

Figure 1 Schematic diagram illustrating the synthesis and energy band diagram of of InP–In_2O_3 p-n junction nanosheet-based porous microspheres (color online).

2.2 Synthesis of InP–In_2O_3

InS-TETA inorganic-organic hybrids were synthesized according to our previously work [44]. In a typical procedure, tartaric acid (2 mmol), $InCl_3$ (1 mmol) and L-cysteine (6 mmol) were added into a mixture solvent of DIW and TETA with a total volume of 18 mL (V_{DIW}/V_{TETA}=2:1) in a 50 mL Teflon-lined stainless-steel autoclave. After stirring to form a homogeneous solution, the autoclave was sealed and treated at 160 °C for 24 h. Then, it was cooled down naturally to room temperature. The white precipitate was washed by DIW and absolute ethanol, respectively, and dried in a vacuum oven to produce InS-TETA.

A 10 mg as-prepared InS-TETA was put into a solvent of 12 mL DIW in a 20 mL Teflon-lined stainless-steel autoclave under stirring to form a homogeneous solution. The autoclave was sealed and kept at 180 °C for 10 h. The yellow precipitate was washed by DIW and absolute ethanol, respectively, and dried in a vacuum oven to produce hierarchical porous In_2S_3 microsphere.

A 50 mg as-prepared hierarchical porous In_2S_3 microsphere was put into a tube furnace. Then, the sample was heated to 500 °C with a rate of 1 °C/min, and kept at 500 °C for 3 h under flowing air atmosphere. Finally, it was cooled down naturally to room temperature to produce hierarchical porous In_2O_3 microsphere.

InP–In_2O_3 was synthesized by gas-solid reaction using sodium hypophosphite as phosphorus source [45]. First, 10 mg as-prepared In_2O_3 and 5 mg $NaH_2PO_2•H_2O$ were put in two separate quartz boats with $NaH_2PO_2•H_2O$ at the upstream side for the furnace. Subsequently, the samples were heated to 300 °C for 1, 2 and 3 h, respectively (see details in Table S1 and Figure S6, Supporting Information online) in a closed Ar atmosphere at a rate of 2 °C/min (take the 2 h sample as example of InP–In_2O_3 mentioned in the text). After cooling down to room temperature, the sample was washed with DIW and absolute ethanol several times, respectively, and finally dried in a vacuum oven overnight.

2.3 Materials characterizations

Powder X-ray diffraction (XRD) was performed on a Bruker D8 Focus Diffraction System (Germany) using a Cu Kα source (λ=0.154178 nm) and the *in-situ* and *ex-situ* X-ray photoelectron spectroscopy (XPS) measurements were performed on a photoelectron spectrometer using Al Kα radiation as the excitation source (PHI 5000 VersaProbe) with or without illumination. All the peaks were calibrated with C 1s spectrum at binding energy of 284.8 eV. Scanning electron microscopy (SEM) and energy disperse spectroscopy (EDS) analysis were taken with a Hitachi S-4800 scanning electron microscope (Japan) equipped with the Thermo Scientific energy-dispersion X-ray fluorescence analyser (USA). Transmission electron microscopy (TEM), high resolution TEM (HRTEM) and scanning transmission electron microscope EDS (STEM-EDS) element mapping images were obtained with Tecnai G2 F20 system equipped with EDAX. UV-Vis diffuse reflectance absorbance spectrum was tested on Shimadzu UV3600 (Japan). The gas chromatograph-mass spectrometer (GC-MS) was carried out with TRACE DSQ. The liquid phase product was measured on Aglient 7890A (USA) with thermal conductivity (TCD) and flame ionization detector (FID). Nuclear magnetic resonance (NMR) spectra were recorded on Varian Mercury Plus 400 instruments (USA) at 400 MHz (^{1}H NMR) and 100 MHz (^{13}C NMR). Chemical shifts were reported in parts per million (ppm) down field from internal tetramethysilane. Multiplicity was indicated as follows: s (singlet), d (doublet), t (triplet), q (quartet), mm (multiplet), dd (doublet of doublet), br (broad). Coupling constants were reported in Hz. The injection temperature was set at 280 °C. Nitrogen was used as the carrier gas at 1.5 mL/min. The gas phase product was measured on Shimadzu GC-2010 Plus (Japan) with barrier discharge ionization detector (BID). The electron spin resonance (ESR) analysis was obtained with Bruker A300 and 300 W Xe lamp (Germany) with the light intensity of 500 mW/cm^2 in the wavelength region of 320–780 nm.

2.4 Photocatalytic CO_2 reduction

The CO_2 photocatalytic reduction is performed in a non-proton environment using Sneaker bottle, which could avoid the competition hydrogen evolution reaction and improve the energy conversion efficiency for CO_2 reduction. In a typical procedure of photocatalytic CO_2 reduction, 25 mg photocatalyst was well-dispersed in CO_2 purged mixture solution of 25 mL acetonitrile and 0.02 mmol THIQ. 300 W Xe lamp with the light intensity of 500 mW/cm^2 in the wavelength region of 320–780 nm was used as the light source. To eliminate the thermal effect, condensate water (25 °C) was introduced to cooling down the system. The generated CO was characterized and quantified by GC-2010 Plus with BID using the following equation. The measurement of the THIQ conversion was discussed later.

The evolution rate of CO were calculated using the equation of

$$\text{Evolution rate } (\mu\text{mol}/(\text{g h})) = \frac{\text{Peak area of CO} \times C}{\text{Peak area of standard gas} \times t \times m} \times V \quad (1)$$

where C is the concentration of CO in standard gas, t is the illumination time, m is the mass of used catalyst, and V is the volume of used Sneaker bottle.

3 Results and discussion

3.1 Morphology and structural characterization

Nanosheet-based porous hierarchical In_2O_3 spheres were synthesized by air oxidation of the corresponding In_2S_3 precursors [45]. Then, the partial phosphating process was carried out by gas-solid reaction using sodium hypophosphite as the phosphorus source (see the details in the Supporting Information online). The SEM images (Figures S1–S3) show the successful preparation of nanosheet-based porous hierarchical In_2O_3 spheres. After phosphating, the hierarchical porous morphology of In_2O_3 can be maintained (Figure 2(a)). The TEM image (Figure 2(b)) indicates the nanosheet-based morphology of as-prepared materials. In the HRTEM image (Figure 2(c)), the fringe spacing of 0.42 nm matches well with the (211) lattice plane of In_2O_3, and some amorphous parts can be clearly seen (the red circle in Figure 2(c)). The amorphous region may be caused by phosphatization. After crystallization at elevated temperature in Ar atmosphere, all the fringe spacings can be attributed to the mixture of In_2O_3 and InP (Figure 2(d)), revealing the heterogeneous components of In_2O_3 and InP rather than P-doping structure. Such hybrid InP–In_2O_3 structure is confirmed later by its Z-scheme photocatalytic mechanism. Although the exact reason for the formation of heterogeneous materials is still unclear, the InP–In_2O_3 hybrids may be associated with the InP–In_2O_3 interface energy and the elastic repulsion between neighboring In_2O_3, as discussed in the initial randomly distributed Ag_2S small islands on CdS during the partial cation exchange reaction of CdS nanorods with Ag^+ cations [46]. The high-angle annular dark field (HAADF) image and the associated STEM-EDS element mapping images (Figure 2(e)) suggest the existence of phosphorus element in the samples. All the XRD peaks are found to originate from cubic In_2O_3 (JCPDS NO.06-0416) (Figure 2(f)). After crystallization, some weak peaks indexed to cubic InP (JCPDS NO.32-0452) can be seen (Figure S4), confirming the compositions of InP and In_2O_3 in the samples. XPS is introduced to verify the element valence state of as-converted samples (Figure 2(g) and Figure S5). For InP–

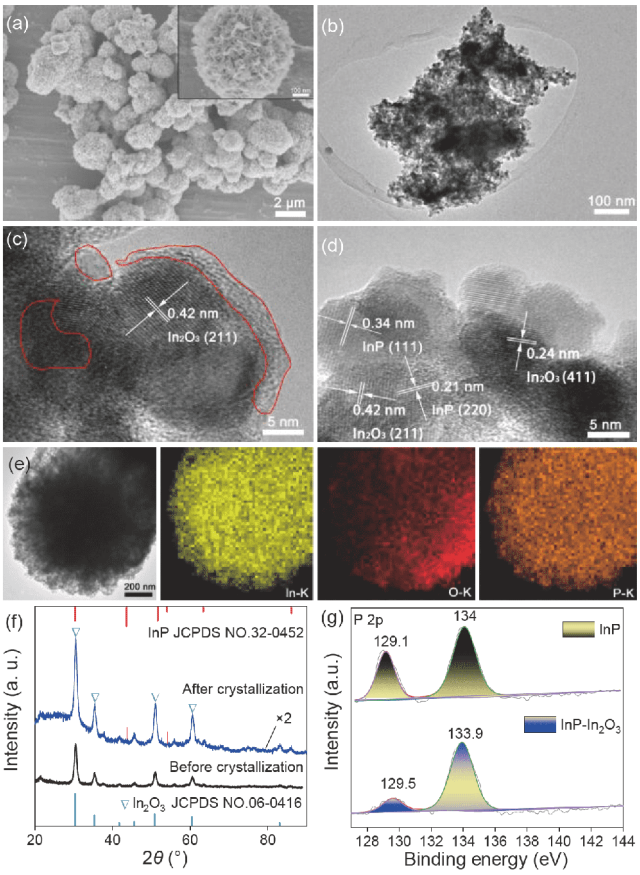

Figure 2 (a) SEM and (b) TEM images of InP–In_2O_3; (c, d) HRTEM images of InP–In_2O_3 before and after crystallization; (e) HAADF and STEM-EDS elemental mapping images of InP–In_2O_3; (f) XRD patterns of InP–In_2O_3 before and after crystallization; (g) P 2p XPS spectra of InP and InP–In_2O_3 (color online).

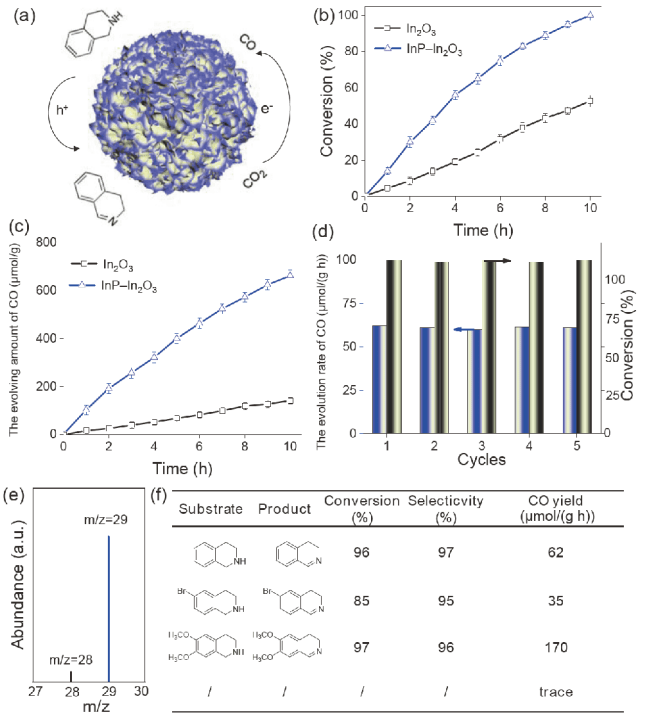

Figure 3 (a) Cartoon integrating the photocatalytic reduction reaction of CO_2 with the oxidative dehydrogenation of tetrahydroisoquinoline over InP–In_2O_3; (b) time-dependent THIQ conversion rates and (c) the evolving amount of CO over In_2O_3 and InP–In_2O_3; (d) cycle tests of InP–In_2O_3 for both CO_2 reduction and THIQ conversion; (e) mass spectra of GC-MS analysis in $^{13}CO_2$ isotope experiment; (f) performance comparisons of THIQ and its derivatives measured after 10 h (color online).

In_2O_3, the peak located at 129.5 eV can be ascribed to P^{3-}. The slightly shift toward higher binding energy of InP–In_2O_3 than InP, which was caused by the surrounding O atoms with stronger electronegativity [47], and the weak peak intensity compared with the pure InP indicated the partial phosphating of the initial In_2O_3. All the aforementioned results demonstrate the successful preparation of InP–In_2O_3.

3.2 Photocatalytic performance

The PRC was performed under the illumination of 300 W Xe lamp (see Supporting Information online for details). As shown in Figure 3(a), the photogenerated electrons and holes from exited InP–In_2O_3 are used to reduce CO_2 and oxidize THIQ, respectively. During the irradiation, the evolving amount of CO, and the conversion of THIQ and its oxidative product were monitored by gas chromatography. For comparison, the performance of In_2O_3 was also evaluated (see details in Table S1 and Figure S9(a–c)). As displayed in Figure 3(b), 0.02 mmol THIQ can be alomost completely converted after 10 h illumination over InP–In_2O_3, superior to that of pure In_2O_3. The oxidation product of THIQ is DHIQ, which is determined by NMR spectrum and GC spectrometry and the selectivity of DHIQ is up to 97% (Figures S11 and S12). Meanwhile, the amount of CO over In_2O_3 and InP–In_2O_3 shows nearly linear growth to 178 and 663 μmol/g, respectively (Figure 3(c)). In addition, the ratio of reduction product/oxidation product is 0.93, which is slightly deviated from 1 due to the deviation of manual injection. Besides, no obvious CO can be detected without THIQ (Figure 3(f)), illustrating the boosted CO_2-to-CO conversion reaction in the presence of THIQ. Furthermore, the photocatalytic activity of InP–In_2O_3 is retained after five runs (Figure 3(d)), suggesting a good stability of the as-pyepared catalyst (Figures S14 and S15). The rates of CO production and conversion of THIQ are kept at about 62 μmol/(g h) and 92%, respectively, suggesting the robust durability of InP–In_2O_3. To verify the carbon source of CO formation, $^{13}CO_2$ isotope experiment was carried out. The results of mass spectrometry show that ^{13}CO (m/z=29) is detected once CO_2 is replaced by $^{13}CO_2$, indicating the carbon atom of evolved CO originates from CO_2 feedstock (Figure 3(e)). In addition, when using Ar as the reaction gas, CO cannot be detected, further confirming that CO product stems from PRC.

To investigate the substrate tolerance, 6-Br- and 6,7-dimethoxy-THIQ were selected as the representative electro-

withdrawing and -donating groups, respectively. Impressively, THIQ with electro-withdrawing or -donating groups can either be facilely oxidized and show an extremely acceptable conversion and high selectivity, simultaneously. And the CO yield can reach 170 μmol/(g h) for 6,7-dimethoxy-THIQ, suggesting the evolution rate of CO_2-to-CO can be accelerated by suitable THIQ derivatives (Figure 3 (f)).

3.3 Electron transfer and mechanism

A series of characterizations were adopted to elucidate the enhanced PRC performance of InP–In_2O_3 in the presence of THIQ. First, UV-Vis diffuse reflectance absorbance spectra (Figure S13) shows that InP–In_2O_3 owns stronger absorbance of visibile light than In_2O_3. Then, transient photocurrent response curves indicate that InP–In_2O_3 shows enhanced photocurrent than In_2O_3, indicating higher separation efficiency of photogenerated electron-hole pairs in InP–In_2O_3 (Figure S9(d)). In addtion, oxygen vacancies can be observed for both In_2O_3 and InP–In_2O_3 samples (Figures S6 and S7), indicating that the improved performance of the InP–In_2O_3 p-n junction do not originate from the presence of oxygen vacancies. The positions of conduction or valance band (CB or VB) of In_2O_3 and InP were measured using Mott-Schottky plots (Figures S8 and S10) [48,49]. Next, some control experiments are carried out to show the photocatalytic mechanism of p-n junction. Firstly, *in situ* irradiated XPS [50] was carried out. After illumination, O 1s peak does positively shift from 531.7 to 531.8 eV (Figure 4 (a)), indicating the decrease of electron density of In_2O_3. At the same time, the characteristic peak of P^{3-} corresponding to InP experience a slightly negative shift of 0.1 eV after illumination, indicating an increase in the electron density of InP. These *in situ* irradiated XPS results provide a solid proof for the In_2O_3-to-InP tranfer of photoelectrons, which is in good agreement with the Z-scheme mechanism. To further verify the interfacial electron tranfer mode, the ESR analysis was implemented to disclose the spin reactive •OH and $•O_2^-$ species motivated by the photocatalysts in water/methanol by using 5,5-dimethyl-1-pyrroline N-oxide (DMPO) as a spin trap [51,52]. It can be seen the DMPO-•OH characteristic peaks generated under UV-Visible light in Figure 4(d). The ESR spectra with relative intensities of 1:2:2:1 indentified to DMPO-•OH addition compound were distinctly detected for both In_2O_3 and InP–In_2O_3, nevertheless, no clearly signal could be observed for InP. Similarly, as shown in Figure 4(c), the DMPO-$•O_2^-$ signals were also tested under UV-Vis irradiation and six characteristic peaks with similar strength were only detected for InP and InP–In_2O_3. Considering the way of electron tranfer, the formation of both $•O_2^-$ and •OH on InP–In_2O_3 should be forbidden if the heterojunction follows the type-II rules as shown in Figure 4(e).

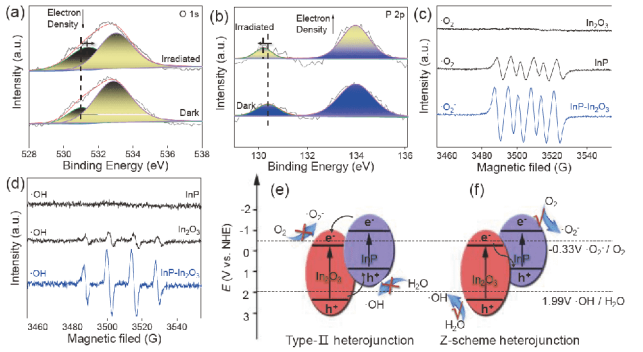

Figure 4 (a, b) *In situ* irradiated XPS spectra of O 1s (a) and P 2p (b) in InP–In_2O_3. (c, d) DMPO spin-trapping ESR spectra recorded for $•O_2^-$ and •OH under UV-Vis light for InP, In_2O_3, InP-In_2O_3; (e, f) schematic illustration of the electron tranfer mode of Type-II and Z-scheme heterojunction for InP–In_2O_3 (color online).

However, for InP–In_2O_3, the intensities of $•O_2^-$ and •OH were both detected. These characteristics suggested that our photocatalytic process follows a Z-scheme mechanism (Figure 4(f)), which is in accordance with *in situ* irradiated XPS observations. Moreover, the signals of both DMPO-•OH and DMPO-$•O_2^-$ that motivated by InP–In_2O_3 were much stronger than the signal of InP and In_2O_3, which indicated that the Z-scheme system exists much higher separate and tranfer efficiency. Therefore, the fabrication of a Z-scheme system in InP–In_2O_3 p-n junction, rather than type-II heterojunction, is a rational reason for boosting the CO_2-to-CO reaction by coupling with THIQ oxidation.

Based on above results, a plausible photocatalytic mechanism for coupling the CO_2-to-CO reaction with the THIQ photooxidation over InP–In_2O_3 is proposed in Scheme 1. The transfer of charge carriers in Z-scheme InP–In_2O_3 is shown in Figure 1, which is endowed the prolonged lifetime of photogenerated carriers to boost surface chemical reaction. For details, the photogenerated holes from In_2O_3 oxidize the THIQ to the associated cation radical **A**, which is subsequently deprotonated to form intermediate **B** (a radical anion). After taking off another proton and releasing one electron, the target product (DHIQ) is acquired. As reported in previous work [35], the released protons can be reduced by the electron from InP to generate H_2. However, only little amount of H_2 was detected in our system. It is well known that a single electron transfer process is undergone to form surface adsorbed $CO_2^{•-}$ in the first step of CO_2 reduction reaction [16], which will abide further reaction with electrons and protons [31]. According to the aforementioned information and our experimental results, we make a reasonable inference that the released protons from THIQ and photogenerated electrons will attack the $CO_2^{•-}$ to form CO and H_2O. The Z-scheme system fabricated by InP–In_2O_3 and the presence of THIQ are responsible for boosting CO_2-to-CO conversion reaction, and simultaneously yielding value-added DHIQ with high selectivity.

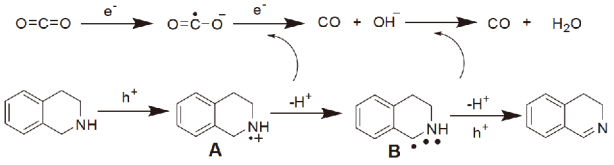

Scheme 1 Proposed mechanism for coupling the photoreduction of CO_2 with the selective photooxidation of tetrahydroisoquinoline over InP–In_2O_3.

4 Conclusions

In summary, a facile *in situ* partial phosphating method has been developed to synthesize InP–In_2O_3 p-n junction for photocatalytic conversion CO_2 to CO with 92% selectivity. The CO evolution rate can be boosted after integrating with the dehydrogenation of THIQ derivatives. Such photooxidation reaction of THIQ can lead to the highly selective formation of DHIQ. After decorated with electron-donating groups, the evolution rates of both CO and dehydrogenation product can be increased, and reach to 170 and 200 μmol/(g h) for CO and the dehydrogenation product of 6,7-dimethoxy-1,2,3,4-THIQ, respectively. Such excellent performances are attributed to the efficient separation/transfer caused by the Z-scheme mechanism of nanosheet-based InP–In_2O_3 p-n junction. Our work may not only provide new opportunities for both CO_2 conversion and DHIQ derivatives with excellent selectivity and high economic value, but also open up a promising method of THIQ derivatives to replace oxygen evolution reaction or sacificant agents during CO_2 conversion reaction.

Acknowledgements This work was supported by the National Natural Science Foundation of China (21422104), and the Natural Science Foundation of Tianjin City (17JCJQJC44700, 16JCZDJC30600).

Conflict of interest The authors declare that they have no conflict of interest.

Supporting information The supporting information is available online at http://chem.scichina.com and http://link.springer.com/journal/11426. The supporting materials are published as submitted, without typesetting or editing. The responsibility for scientific accuracy and content remains entirely with the authors.

1 Gao S, Lin Y, Jiao X, Sun Y, Luo Q, Zhang W, Li D, Yang J, Xie Y. *Nature*, 2016, 529: 68–71
2 Gao C, Chen S, Wang Y, Wang J, Zheng X, Zhu J, Song L, Zhang W, Xiong Y. *Adv Mater*, 2018, 30: 1704624
3 Zhang A, He R, Li H, Chen Y, Kong T, Li K, Ju H, Zhu J, Zhu W, Zeng J. *Angew Chem Int Ed*, 2018, 57: 10954–10958
4 Zeng G, Qiu J, Hou B, Shi H, Lin Y, Hettick M, Javey A, Cronin SB. *Chem Eur J*, 2015, 21: 13502–13507
5 Bushuyev OS, De Luna P, Dinh CT, Tao L, Saur G, van de Lagemaat J, Kelley SO, Sargent EH. *Joule*, 2018, 2: 825–832
6 Cammarota RC, Vollmer MV, Xie J, Ye J, Linehan JC, Burgess SA, Appel AM, Gagliardi L, Lu CC. *J Am Chem Soc*, 2017, 139: 14244–14250
7 Neaţu Ş, Maciá-Agulló JA, Concepción P, Garcia H. *J Am Chem Soc*, 2014, 136: 15969–15976
8 Wang S, Guan BY, Lu Y, Lou XW. *J Am Chem Soc*, 2017, 139: 17305–17308
9 Wang J, Li G, Li Z, Tang C, Feng Z, An H, Liu H, Liu T, Li C. *Sci Adv*, 2017, 3: e1701290
10 Kang Q, Wang T, Li P, Liu L, Chang K, Li M, Ye J. *Angew Chem Int Ed*, 2015, 54: 841–845
11 Teramura K, Iguchi S, Mizuno Y, Shishido T, Tanaka T. *Angew Chem Int Ed*, 2012, 51: 8008–8011
12 Oshima T, Ichibha T, Qin KS, Muraoka K, Vequizo JJM, Hibino K, Kuriki R, Yamashita S, Hongo K, Uchiyama T, Fujii K, Lu D, Maezono R, Yamakata A, Kato H, Kimoto K, Yashima M, Uchimoto Y, Kakihana M, Ishitani O, Kageyama H, Maeda K. *Angew Chem Int Ed*, 2018, 57: 8154–8158
13 Cao S, Shen B, Tong T, Fu J, Yu J. *Adv Funct Mater*, 2018, 28: 1800136
14 Yu L, Li G, Zhang X, Ba X, Shi G, Li Y, Wong PK, Yu JC, Yu Y. *ACS Catal*, 2016, 6: 6444–6454
15 Jia J, O'Brien PG, He L, Qiao Q, Fei T, Reyes LM, Burrow TE, Dong Y, Liao K, Varela M, Pennycook SJ, Hmadeh M, Helmy AS, Kherani NP, Perovic DD, Ozin GA. *Adv Sci*, 2016, 3: 1600189
16 Pan YX, You Y, Xin S, Li Y, Fu G, Cui Z, Men YL, Cao FF, Yu SH, Goodenough JB. *J Am Chem Soc*, 2017, 139: 4123–4129
17 Shi H, Chen G, Zhang C, Zou Z. *ACS Catal*, 2014, 4: 3637–3643
18 Zeng G, Qiu J, Li Z, Pavaskar P, Cronin SB. *ACS Catal*, 2014, 4: 3512–3516
19 Li F, Chen L, Xue M, Williams T, Zhang Y, MacFarlane DR, Zhang J. *Nano Energy*, 2017, 31: 270–277
20 Hong D, Tsukakoshi Y, Kotani H, Ishizuka T, Kojima T. *J Am Chem Soc*, 2017, 139: 6538–6541
21 Nakada A, Nakashima T, Sekizawa K, Maeda K, Ishitani O. *Chem Sci*, 2016, 7: 4364–4371
22 Kuehnel MF, Orchard KL, Dalle KE, Reisner E. *J Am Chem Soc*, 2017, 139: 7217–7223
23 Ran J, Jaroniec M, Qiao SZ. *Adv Mater*, 2018, 30: 1704649
24 Wei N, Cui H, Song Q, Zhang L, Song X, Wang K, Zhang Y, Li J, Wen J, Tian J. *Appl Catal B-Environ*, 2016, 198: 83–90
25 He H, Lin J, Fu W, Wang X, Wang H, Zeng Q, Gu Q, Li Y, Yan C, Tay BK, Xue C, Hu X, Pantelides ST, Zhou W, Liu Z. *Adv Energy Mater*, 2016, 6: 1600464
26 Hong X, Kim J, Shi SF, Zhang Y, Jin C, Sun Y, Tongay S, Wu J, Zhang Y, Wang F. *Nat Nanotech*, 2014, 9: 682–686
27 Wang H, Zhang L, Chen Z, Hu J, Li S, Wang Z, Liu J, Wang X. *Chem Soc Rev*, 2014, 43: 5234–5244
28 Zhou P, Yu J, Jaroniec M. *Adv Mater*, 2014, 26: 4920–4935
29 Li H, Tu W, Zhou Y, Zou Z. *Adv Sci*, 2016, 3: 1500389
30 Roske CW, Popczun EJ, Seger B, Read CG, Pedersen T, Hansen O, Vesborg PCK, Brunschwig BS, Schaak RE, Chorkendorff I, Gray HB, Lewis NS. *J Phys Chem Lett*, 2015, 6: 1679–1683
31 Habisreutinger SN, Schmidt-Mende L, Stolarczyk JK. *Angew Chem Int Ed*, 2013, 52: 7372–7408
32 Tian J, Zhao Z, Kumar A, Boughton RI, Liu H. *Chem Soc Rev*, 2014, 43: 6920–6937
33 Sabaté J, Cerveramarch S, Simarro R, Gimenez J. *Int J Hydrogen Energy*, 1990, 15: 115–124
34 Chen X, Shen S, Guo L, Mao SS. *Chem Rev*, 2010, 110: 6503–6570
35 Zheng M, Shi J, Yuan T, Wang X. *Angew Chem Int Ed*, 2018, 57: 5487–5491
36 Zhao W, Liu C, Cao L, Yin X, Xu H, Zhang B. *RSC Adv*, 2013, 3: 22944–22948
37 Kamat PV, Jin S. *ACS Energy Lett*, 2018, 3: 622–623
38 Han G, Jin YH, Burgess RA, Dickenson NE, Cao XM, Sun Y. *J Am Chem Soc*, 2017, 139: 15584–15587
39 He KH, Zhang WD, Yang MY, Tang KL, Qu M, Ding YS, Li Y. *Org Lett*, 2016, 18: 2840–2843
40 Huang C, Huang Y, Liu C, Yu Y, Zhang B. *Angew Chem Int Ed*, 2019, 58: 12014–12017

41 Kim DS, Park JW, Jun CH. *Adv Synth Catal*, 2013, 355: 2667–2679
42 Wu J, Talwar D, Johnston S, Yan M, Xiao J. *Angew Chem Int Ed*, 2013, 52: 6983–6987
43 Niu YN, Yan ZY, Gao GL, Wang HL, Shu XZ, Ji KG, Liang YM. *J Org Chem*, 2009, 74: 2893–2896
44 Wu R, Xu Y, Xu R, Huang Y, Zhang B. *J Mater Chem A*, 2015, 3: 1930–1934
45 Zhang C, Huang Y, Yu Y, Zhang J, Zhuo S, Zhang B. *Chem Sci*, 2017, 8: 2769–2775
46 Robinson RD, Sadtler B, Demchenko DO, Erdonmez CK, Wang LW, Alivisatos AP. *Science*, 2007, 317: 355–358
47 Yu Y, Huang Y, Yu Y, Shi Y, Zhang B. *Nano Energy*, 2018, 43: 236–243
48 Liu G, Karuturi SK, Chen H, Spiccia L, Tan HH, Jagadish C, Wang D, Simonov AN, Tricoli A. *Nano Energy*, 2018, 53: 745–752
49 Liu Y, Li J, Li W, Yang Y, Li Y, Chen Q. *J Phys Chem C*, 2015, 119: 14834–14842
50 Low J, Dai B, Tong T, Jiang C, Yu J. *Adv Mater*, 2019, 31: 1802981
51 Jiang Z, Wan W, Li H, Yuan S, Zhao H, Wong PK. *Adv Mater*, 2018, 30: 1706108
52 Li H, Qin F, Yang Z, Cui X, Wang J, Zhang L. *J Am Chem Soc*, 2017, 139: 3513–3521